INAF
ISTITUTO NAZIONALE
DI ASTROFISICA
NATIONAL INSTITUTE
FOR ASTROPHYSICS

Publication Year	2021
Acceptance in OA	2025-02-24T11:10:30Z
Title	Dissecting nonthermal emission in the complex multiple-merger galaxy cluster Abell 2744: Radio and X-ray analysis
Authors	Rajpurohit, K., VAZZA, Franco, van Weeren, R. J., Hoeft, M., BRIENZA, Marisa, Bonnassieux, E., Riseley, C. J., BRUNETTI, Gianfranco, BONAFEDE, Annalisa, Brüggen, M., Formann, W. R., Rajpurohit, A. S., Röttgering, H. J. A., Drabent, A., Domínguez-Fernández, P., Wittor, D., Andrade-Santos, F.
Publisher's version (DOI)	10.1051/0004-6361/202141060
Handle	http://hdl.handle.net/20.500.12386/36154
Journal	ASTRONOMY & ASTROPHYSICS
Volume	654

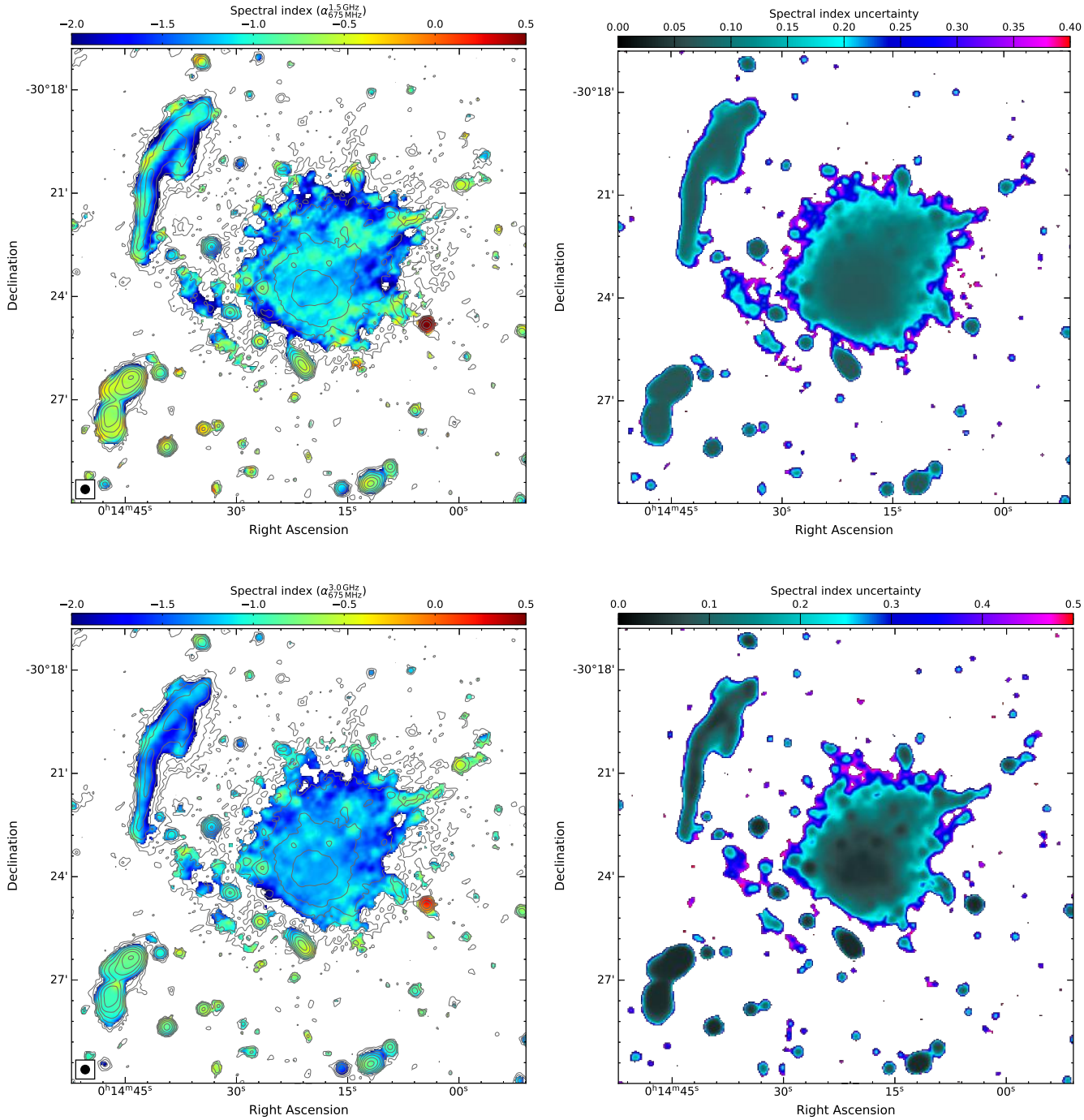

Fig. 9. *Left*: spectral index maps of the halo between 675 MHz and 1.5 GHz (*top*) and 675 MHz and 3.0 GHz (*bottom*) at 15″ resolution. The image properties are given in Table 2, IM3, IM7, and IM13. Contour levels are drawn at $[1, 2, 4, 8, \ldots] \times 3.5\,\sigma_{\mathrm{rms}}$, and are from the uGMRT Band 4 image. These maps show the presence of steeper spectral indices in outermost regions of the halo, in particular to the north. *Right*: corresponding spectral index uncertainty.

innermost regions also show variations from about 4 keV to 10 keV (Pearce et al. 2017).

Moreover, the spectral index gets steeper in the outermost regions, in particular in the northern part of the halo. According to the reaccelerations models, such steeper indices are expected in the simplified situation where the acceleration rate is constant due to the decline in the magnetic field with radius for $B^2 \ll B^2_{\mathrm{CMB}}$ (Brunetti et al. 2001). The spectral index trends are similar for indices derived between 675 MHz and 1.5 GHz and between 675 MHz and 3 GHz, see Fig. 9.

Pearce et al. (2017) studied the spectral variations across the radio halo between 1.5 and 3 GHz. They found that the spectral distribution is more or less uniform across the halo with $\langle\alpha\rangle = -1.37$ and standard deviation of $\sigma = 0.28$. In the left panel of Fig. 10, we show the histogram of the spectral index distribution from 675 MHz to 1.5 GHz and 675 MHz to 3 GHz, extracted from 15″ resolution maps. Between 675 MHz and 1.5 GHz, the spectral index distribution shows the median spectral index of $\langle\alpha^{1.5\,\mathrm{GHz}}_{675\,\mathrm{MHz}}\rangle = -1.15$ and a standard derivation of $\sigma_{15''} = 0.18$. This value is consistent with the integrated spectral index of the

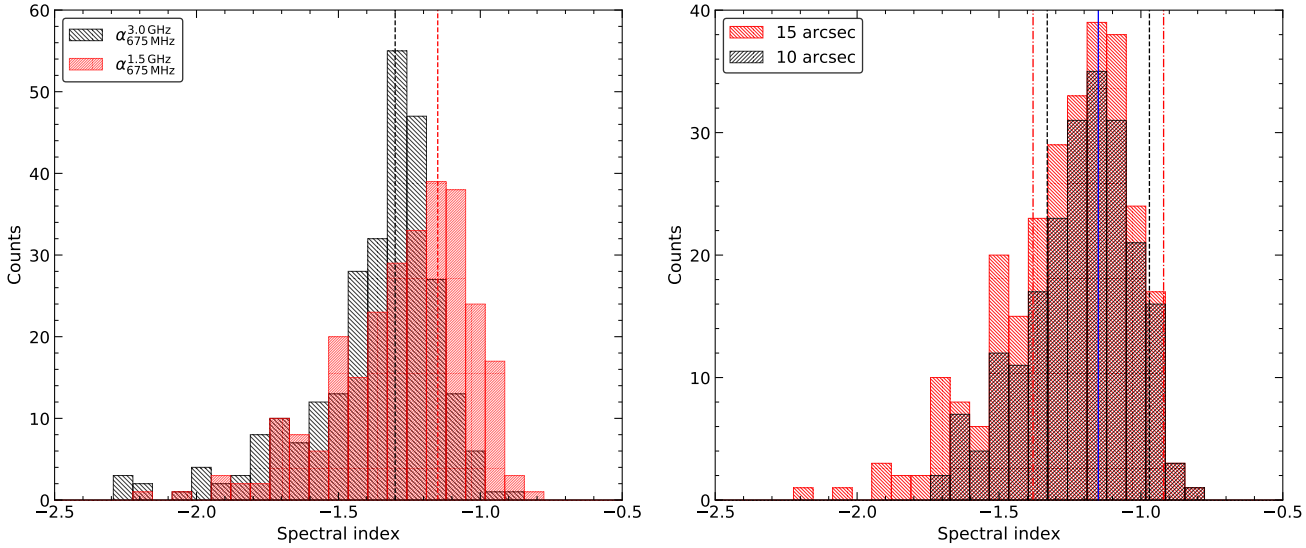

Fig. 10. *Left*: histogram of the spectral index distribution across the halo in Abell 2744 for different sets of frequencies. The low frequency values were obtained between 675 MHz and 1.5 GHz (in red) while the other one between 675 MHz and 3 GHz (in black). The spectral indices were extracted from 15″ boxes, corresponding to a physical size of about 67 kpc. The dashed lines represent the median spectral index values. *Right*: histogram of spectral index values obtained from 10″ (black) and 15″ (red) resolution radio maps created between 675 MHz and 1.5 GHz. The plot suggest that the distribution of the mean spectral index and its standard deviation have a little impact when adopting different resolutions. The solid blue line represents the median value, $\langle\alpha\rangle = -1.15$, at both 10″ and 15″ resolution. The dash-dotted (red) and dashed (black) lines represent the standard deviation around the median values at 10″ ($\sigma_{10''} = 0.19$) and 15″ ($\sigma_{15''} = 0.24$), respectively.

halo, namely -1.14 ± 0.05. Between 675 MHz and 3 GHz, we measure a median value of $\langle\alpha^{3.0\,\mathrm{GHz}}_{675\,\mathrm{MHz}}\rangle = -1.31$ and $\sigma_{15''} = 0.24$, which is comparable with those reported by Pearce et al. (2017) between 1.5 and 3 GHz.

At 15″, we measure the median spectral index uncertainty of 0.15 and 0.10 between 675 MHz and 1.5 GHz and 675 MHz and 3.0 GHz, respectively. If the variations in the spectral index are the result of measurement uncertainties, the median uncertainty is expected to be comparable to the standard deviation. The median error between 675 MHz and 3.0 GHz is about 2.4 times the standard deviation, hinting at a small-scale spectral index fluctuation across the halo as found for radio halos in Abell 2255 (Botteon et al. 2020a), Abell 520 (Vacca et al. 2014; Hoang et al. 2019), and MACS J0717.5+3745 (Rajpurohit et al. 2021a). In the latter case, it was suggested that the large scatter around the average spectral index is due to strong inverse Compton (IC) losses because of the high redshift of that cluster. At high redshift, IC losses are strong and the electron acceleration could produce synchrotron emission preferentially in regions with $B \sim B_{\mathrm{CMB}}$, whereas the acceleration process is quenched where turbulence is lower. We emphasize that the other two clusters are located at a relatively low redshift. The fluctuations in the spectral index across the halo are expected in turbulent reacceleration models caused by magnetic field variations and different (re-)acceleration efficiency within the halo (e.g., Brunetti et al. 2001; Petrosian 2001; Brunetti & Lazarian 2007). In contrast, the secondary models predict a uniform spectral index distribution due to continuous generation of relativistic electrons through the collision between relativistic protons and thermal protons in the ICM (e.g., Pfrommer et al. 2008; Enßlin et al. 2011).

To check the effect of the cell size on the median spectral index and standard deviation using two different resolutions, 10″ and 15″. As shown in the right panel of Fig. 10, between 675 MHz and 1.5 GHz the mean spectral index remains the same at both resolutions, namely −1.15. The standard deviations at 10″ and 15″ are 0.19 and 0.24, respectively. This indicates that the distribution of the mean value and its standard deviation have little effect when adopting different resolutions.

We also investigate if the halo shows any sign of spectral curvature. The spectral curvature (SC) map was derived as:

$$\mathrm{SC} = -\alpha_{\mathrm{low}} + \alpha_{\mathrm{high}}. \quad (5)$$

We use the 15″ resolution maps at 675 MHz, 1.5 GHz and 3 GHz. The low frequency spectral index map is created between 675 MHz and 1.5 GHz and the high frequency map between 1.5 GHz and 3 GHz. The SC is negative for a convex spectrum. The curvature map of the halo is shown in the left panel of Fig. 11. The halo shows localized regions with a clear curvature.

We also performed the radio color-color analysis for the halo. The regions used for extracting spectral indices are shown in the right panel of Fig. 11 and the resulting color-color plot in the left panel of Fig. 12. The majority of data points lie below the power-law line, a clear sign of negative curvature. No curvature is expected in the secondary models of halo formation because cosmic-ray protons do not lose significant amount of energy, therefore the spectral index remains constant producing a power-law without any curvature (e.g., Dolag & Enßlin 2000; Pfrommer et al. 2008). The number of radio halos where spectral curvature has been measured is still extremely limited. Only for two radio halos has such an analysis been carried out, namely MACS J0717.5+3745 (Rajpurohit et al. 2021a) and 1RXS J0603.3+4214 (Rajpurohit et al. 2020a). The halo in MACS J0717.5+3745 shows a significant curvature while no curvature is found in the 1RXS J0603.3+4214 halo. The curvature distribution across the halo in Abell 2744 is quite different from the MACS J0717.5+3745 halo. Moreover, the curvature distribution seems different in the northern and southern parts of the halo.

It is worth noting the difference in the spectral properties of the halos in Abell 2744, 1RXS J0603.3+4214, and MACS J0717.5+3745. The 1RXS J0603.3+4214 halo shows a

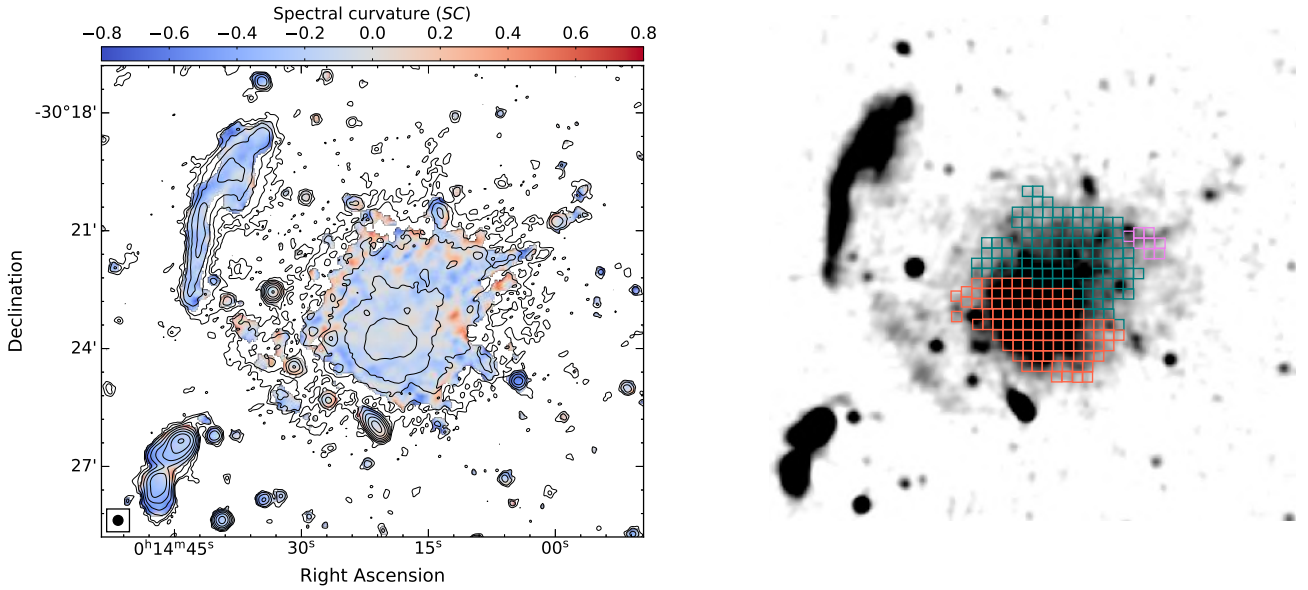

Fig. 11. *Left*: three frequency spectral curvature map of the halo at 15″ resolution, created using 675 MHz, 1.5 GHz, and 3 GHz radio maps. The image properties are given in Table 2, IM3, IM7, and IM13. The halo shows a hint of spectral curvature. The SC is negative for a convex spectrum. Contour levels are drawn at $[1, 2, 4, 8, \ldots] \times 3.5\,\sigma_{\rm rms}$, and are from the uGMRT Band 4 image. *Right*: regions where the radio spectral index values were extracted between 675 MHz and 3 GHz. Each box has a width of 15″ corresponding to a physical size of about 67 kpc. The same regions are used to obtained α–$I_{\rm X}$ correlation in the left panel of Fig. 15.

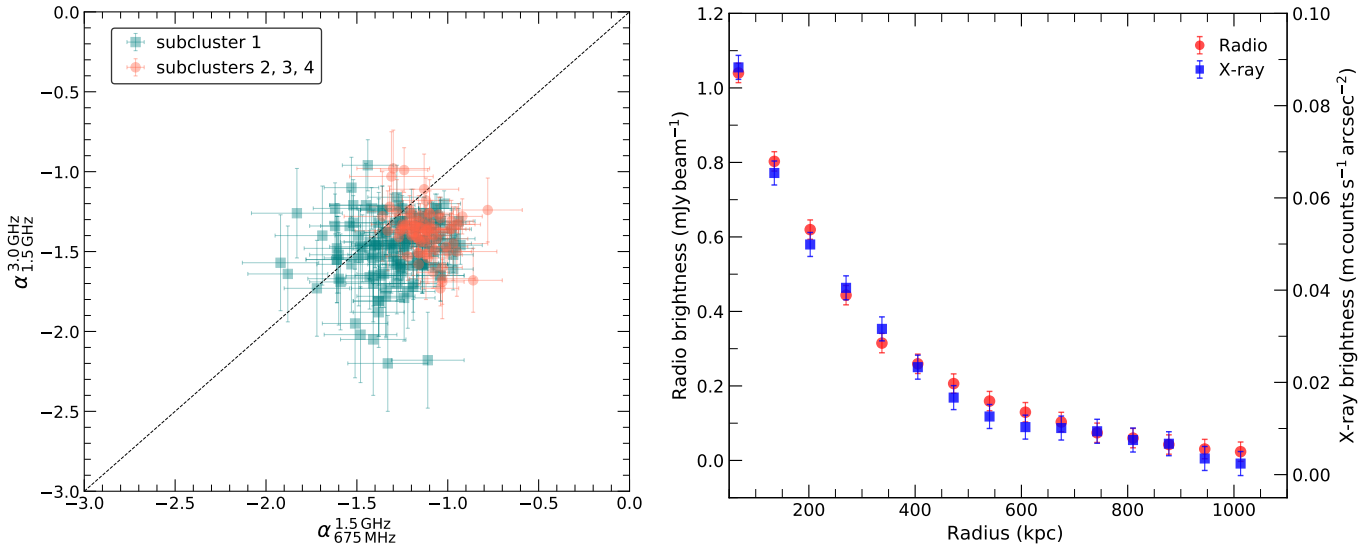

Fig. 12. *Left*: radio color-color plot of the halo, showing a complex spectral curvature distribution. The orange data points are extracted from the southern part of the halo while turquoise one from the northern part. The curvature distribution is seems different in the northern and southern parts of the halo. Regions used for extracting the spectral index values are are shown in the right panel of Fig. 11. *Right*: comparison between the radio (red) and the X-ray (blue) surface brightness profiles for the Abell 2744 halo. The X-radio and X-ray profiles are remarkably similar.

power-law spectrum, a remarkably uniform spectral index distribution, and no spectral curvature (van Weeren et al. 2016; Rajpurohit et al. 2020a) while the one in MACS J0717.5+3745 shows a curved spectrum, strong spectral index fluctuations, steeper spectral indices and curvature in the outermost regions (Rajpurohit et al. 2021a). The present halo, on the other hand shows an overall power-law spectrum with small-scale spectral index fluctuations, steeper spectral index in the outermost regions and a hint of spectral curvature. We conclude that an overall power-law spectrum observed in radio halos does not necessary imply a uniform spectral index distribution. In fact, an overall power-law may be also observed in combination of quite a variety of spectral indices and curvature distributions.

6. X-ray and radio correlations

The similarity between X-ray and radio morphologies of halos in galaxy clusters indicates a connection between the energetics of the nonthermal (magnetic fields and relativistic electrons) and thermal components of the ICM. The morphology of the radio halo is remarkably similar to the X-ray emission in Abell 2744, Fig. 5.

To examine the profiles of the X-ray and radio emission of the halo, we divided the halo into regions of concentric circular annuli centered on the X-ray surface brightness peak (see the right panel of Fig. 6). We used the 15″ 675 MHz radio image. The mean surface brightness and standard deviations were

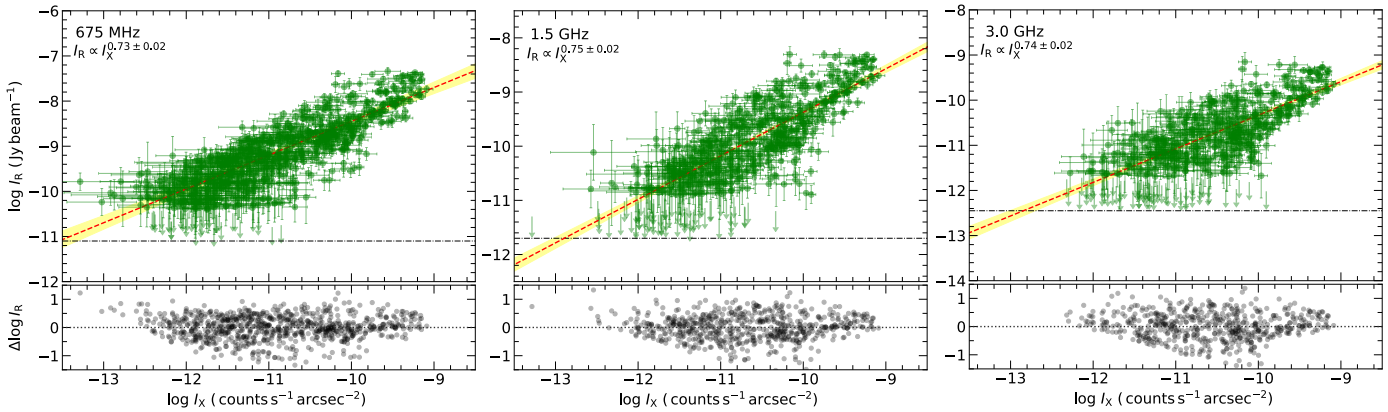

Fig. 13. *Left*: I_R–I_X relation of the halo in Abell 2744, extracted in square boxes with width of 10″ (about 45 kpc). The X-ray surface brightness is extracted from the *Chandra* (0.5–2.0 keV band) image smoothed with a Gaussian FWHM of 3″. The radio surface brightness is extracted from radio maps at 10″ resolution. The `Linmix` best-fit relations are indicated by red dashed lines. Green circles depict cells where the radio and X-ray surface brightness is above 3σ level. The upper limits (arrows) represent cells with data points below 2σ radio noise level. The horizontal black dash-dotted lines indicate the 1σ in the radio maps. Yellow show samples from the posterior distribution. The best-fit are reported with the corresponding 95% confidence regions. *Lower panel*: residuals of log I_R and log I_X with respect to the `Linmix` best fit line. The radio brightness strongly correlates with the X-ray at all three frequencies. The best-fitting slopes at 675 MHz, 1.5 GHz and 3 GHz are 0.73 ± 0.02, 0.75 ± 0.02, and 0.74 ± 0.02, respectively.

estimated within concentric rings. The discrete sources (both from radio and X-ray images) and the relics R2, R3, and R4 were masked out and were excluded from the analysis. In the right panel of Fig. 12 we show the resulting radial profiles. Despite the fact that the X-ray emission is characterized by the presence of several substructure, the radio and X-ray brightness matches quite well, as also reported by Govoni et al. (2001a). Both, radio and X-ray brightness falls rapidly up to a radii of 600 kpc and flatter profile is seen at a radius >600 kpc.

6.1. Spatial correlation between X-ray and radio brightness

For several halos, a point-to-point analysis of radio and X-ray surface brightness has been performed mostly at 1.4 GHz. Most of the halos are reported to show a linear or sublinear correlation at 1.4 GHz (Govoni et al. 2001a,b; Shimwell et al. 2014; Rajpurohit et al. 2018, 2021a; Hoang et al. 2019; Cova et al. 2019; Xie et al. 2020; Botteon et al. 2020a; Bruno et al. 2021). This relationship is generally described by a power law:

$$\log I_R = a + b \log I_X, \quad (6)$$

where the slope b determines whether the thermal components of the ICM (i.e., the thermal gas density and temperature) declines (if $b < 1$) faster than the nonthermal components (i.e., the magnetic fields and relativistic particles) or vice versa (if $b > 1$).

High resolution, sensitive uGMRT, VLA, and *Chandra* X-ray data, allow us to perform a detailed investigation of the interplay between the thermal and nonthermal components of the ICM. We make use of 675 MHz, 1.5 GHz, and 3 GHz radio images created at 10″ resolution, with uniform weighting scheme and a uvcut of 0.2 kλ. The *Chandra* X-ray image was smoothed with a Gaussian FWHM of 3″. We construct a grid covering the entire halo region, excluding R2, R3, R4, and discrete sources. The width of each cell is 10″ (45 kpc). To retain good signal-to-noise, we include those areas where the radio and X-ray surface brightness is above the 3σ level. However, regions where the radio surface brightness is above 2σ are included as an upper limit. The radio brightness is expressed in Jy beam^{-1} and X-ray in counts s^{-1} arcsec^{-2}.

Figure 13 shows the point-to-point comparison between the X-ray and radio brightness at 675 MHz, 1.5 GHz, and 3 GHz. The halo shows a clear positive correlation at all three frequencies: higher radio brightness is associated with higher X-ray brightness, in agreement with Govoni et al. (2001a). We use the `Linmix`[3] package (Kelly 2007) to determine the best-fitting parameters to the observed data. `Linmix` uses a Bayesian hierarchical approach to linear regression considering measurement uncertainties on both axes. It also incorporates nondetection on y-variable (upper limit) and allows the estimation of intrinsic random scatter in the regression. The correlation strength was measured by the Spearman and Pearson correlation coefficients.

In Table 5, we summarize the best-fit slopes and corresponding correlation coefficients for each radio frequency considered here. The I_R and I_X are strongly correlated at 675 MHz, 1.5 GHz, and 3 GHz. We find a sublinear slope of $b_{675\,\mathrm{MHz}} = 0.73 \pm 0.02$, $b_{1.5\,\mathrm{GHz}} = 0.75 \pm 0.02$, and $b_{3\,\mathrm{GHz}} = 0.74 \pm 0.02$ at 675 MHz, 1.5 GHz, and 3 GHz, respectively. A sublinear slope is also found for the radio halos in Abell 2319 (Govoni et al. 2001a), Coma cluster (Govoni et al. 2001a), MACS J0717.5+3745 (Rajpurohit et al. 2021a), MACS J1149.5+2223 (Bruno et al. 2021), and Abell 2163 (Feretti et al. 2001).

As shown in Fig. 13, the number of data points are different at 675 MHz, 1.5 GHz, and 3 GHz, indicating that we are sampling different regions. We note that the range of X-ray surface brightness is smaller at 3 GHz, suggesting the total halo region at 3 GHz is smaller or more central. Therefore, to compare correlations in the same region, we performed a new fitting of the correlations at 675 MHz and 1.5 GHz by including only the boxes used at 3 GHz. This results in the correlation slopes of $b_{675\,\mathrm{MHz}} = 0.77 \pm 0.02$ and $b_{1.5\,\mathrm{GHz}} = 0.78 \pm 0.02$. While these values are marginally steeper than those listed in Table 5, it suggests that the constant and sublinear slope found at 675 MHz, 1.5 GHz, and 3 GHz is independent of regions.

Intriguingly, the slope in the Abell 2744 halo is remarkably uniform, namely 0.73 ± 0.02, 0.75 ± 0.02, and 0.74 ± 0.02 at 675 MHz, 1.5 GHz, and 3 GHz, respectively. Recently, we

[3] https://linmix.readthedocs.io/en/latest/src/linmix.html

Table 5. `Linmix` fitting slopes and Spearman (r_s) and Pearson (r_p) correlation coefficients of the data for Figs. 13 and 14.

	ν	3σ				2σ			
		b	σ_{int}	r_s	r_p	b	σ_{int}	r_s	r_p
Halo	675 MHz	0.67 ± 0.02	0.10 ± 0.01	0.86	0.83	0.73 ± 0.02	0.13 ± 0.01	0.87	0.85
	1.5 GHz	0.71 ± 0.03	0.13 ± 0.01	0.81	0.77	0.75 ± 0.02	0.15 ± 0.01	0.84	0.78
	3.0 GHz	0.66 ± 0.03	0.12 ± 0.01	0.77	0.75	0.74 ± 0.02	0.16 ± 0.02	0.81	0.77
Northern	675 MHz	0.53 ± 0.02	0.05 ± 0.01	0.82	0.78	0.65 ± 0.02	0.08 ± 0.01	0.86	0.78
	1.5 GHz	0.54 ± 0.04	0.07 ± 0.01	0.72	0.71	0.68 ± 0.04	0.11 ± 0.01	0.77	0.81
	3.0 GHz	0.42 ± 0.04	0.05 ± 0.01	0.82	0.71	0.60 ± 0.04	0.10 ± 0.01	0.75	0.64
Southern	675 MHz	0.72 ± 0.02	0.07 ± 0.01	0.92	0.90	0.77 ± 0.02	0.08 ± 0.01	0.94	0.90
	1.5 GHz	0.82 ± 0.02	0.05 ± 0.01	0.88	0.75	0.82 ± 0.02	0.10 ± 0.01	0.92	0.81
	3.0 GHz	0.70 ± 0.06	0.09 ± 0.01	0.84	0.80	0.75 ± 0.03	0.10 ± 0.01	0.90	0.85

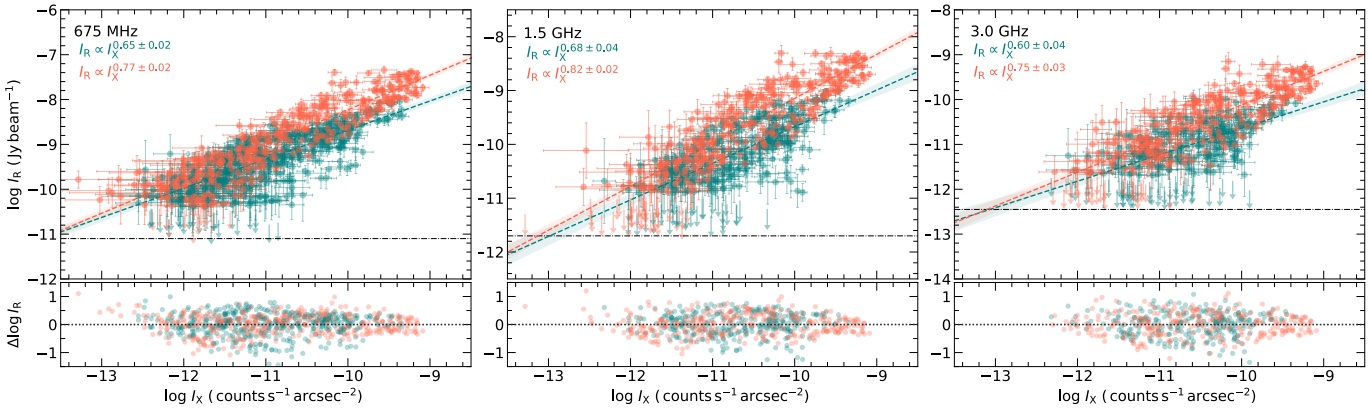

Fig. 14. *Left*: I_R–I_X relation for the northern (turquoise) and southern (orange) parts of the halo. The upper limits (arrows) represent cells with data points below 2σ radio noise level. The horizontal black dash-dotted lines indicate the 1σ in the radio maps. The turquoise and orange dashed lines correspond to the best-fit obtained separately for the northern and southern, respectively, parts of the halo. The best-fits are reported with the corresponding 95% confidence regions. The correlation slope is indeed different for the northern and southern regions of the halo: the southern part of the halo is steeper than the northern part at all three frequencies.

investigated the I_R–I_X relation for the MACS J0717.5+3745 halo at different frequencies (Rajpurohit et al. 2021a). Unlike Abell 2744 halo, the correlation slope in the MACS J0717.5+3745 halo gets steeper toward high frequencies implying a high frequency spectral steepening. As discussed in Sect. 6.3, the halo consists of at least two main components (northern and southern; see Fig. 1), therefore we also fit the data separately to check if these two components show different behavior in the I_R and I_X relation. The resulting plot is shown in Fig. 14 with corresponding best-fitting slopes. Compared to the northern part, the radio emission across the southern part of the halo is strongly correlated with the X-ray surface brightness, see Table 5. In addition, the correlation slope is different for the northern and southern parts, suggesting different cluster dynamics in these regions.

The correlation slope of the southern part of the halo is clearly significantly steeper than the northern part at all three frequencies. It implies that along the denser regions (subclusters 2 and 3) the radio emissivity is enhanced more than the X-ray emissivity. The correlation slope is still relatively uniform as a function of frequency for both the northern and southern parts. The uniform correlation slope in the Abell 2744 halo is may be due to the fact that at 3 GHz, we are not sampling regions with low X-ray brightness.

Our slope at 1.5 GHz is significantly flatter than reported previously by Govoni et al. (2001a), namely $b_{1.4\,GHz} = 0.99 \pm 0.05$. We note that Govoni et al. (2001a) used a Least-Square fitting which may give different results. To check this, we also fit the 1.5 GHz data using Least Squares regression. We emphasize that this regression method is less powerful than `Linmix` since it does not account for measurement uncertainties in both variables and does not provide an estimate of the intrinsic scatter. Using Least-Square fitting, we obtained a slope of 0.80 ± 0.03, still inconsistent with Govoni et al. (2001a).

It is worth noting that Govoni et al. (2001a) used rather low resolution radio (50″) and X-ray (30″) images. We thus repeated the fitting using `Linmix` at 25″ and 50″ resolution images. We created two new grids covering the halo. Each cell size in these grids is similar to the beam of the radio image at these two resolutions. We obtained a slope of $b_{25'',1.5\,GHz} = 0.81 \pm 0.02$ and $b_{50'',1.5\,GHz} = 0.82 \pm 0.02$. This indicates that the correlation slope changes slightly when using low resolution images. The change in the slope is negligible when going from 20″ ($b_{25'',1.5\,GHz} = 0.81 \pm 0.02$) to 50″ ($b_{50'',1.5\,GHz} = 0.82 \pm 0.02$) but the slope is slightly flatter at higher resolution, namely at 10″ ($b_{10'',1.5\,GHz} = 0.75 \pm 0.02$). The same trends are noticed at 675 MHz and 3 GHz. The change in image resolution thus cannot explain the difference in the slope obtained by Govoni et al. (2001a) and ours. Lastly, we fit the low resolution data points using Least Squares regression and also included R2, R3, and R4 regions embedded in the halo. This results in a slope of 0.96 ± 0.03 which is consistent with Govoni et al. (2001a). We conclude that the I_R–I_X correlation slope for the halo in Abell 2744 is indeed sublinear.

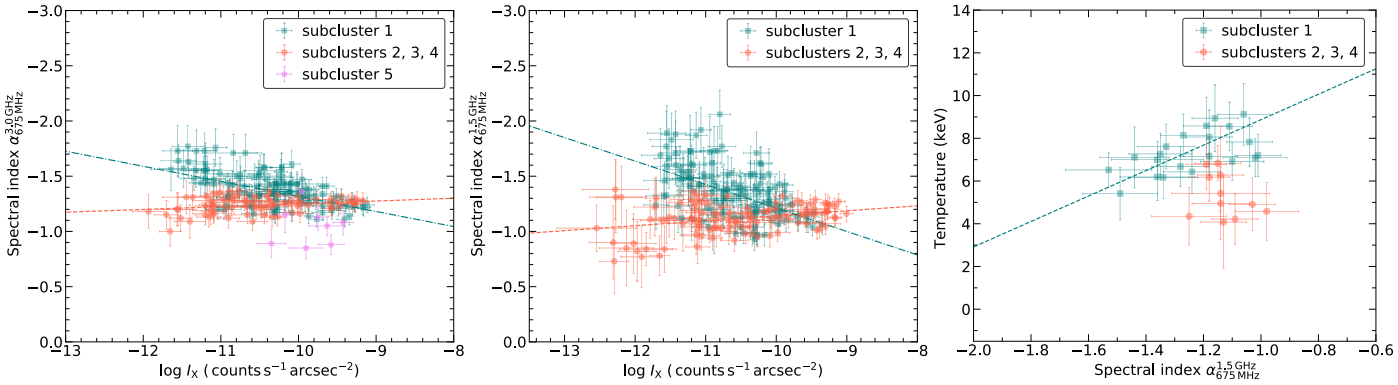

Fig. 15. *Left*: α–I_X relation of the halo in Abell 2744 between 675 MHz and 3 GHz. Regions where the spectral indices were extracted are shown in the right panel of Fig. 11. *Middle*: α–I_X between 675 MHz and 1.5 GHz. The halo shows evidence of two different components with possibly different evolutionary stage. `Linmix` best-fit relations are indicated by dashed lines obtained separately for two different regions. In Table 6, we summarize the best-fit parameters. *Right*: α–T_X relation for the Abell 2744 halo. The spectral index values were extracted in the same regions as used for the X-ray temperature measurements.

The correlation slopes provide information about the different acceleration models and the distribution of magnetic fields (e.g., Dolag & Enßlin 2000; Govoni et al. 2001a; Storm et al. 2015). The radio emissivity due to synchrotron emission, j_R, depends on the number density of relativistic electrons and the magnetic field strength

$$j_R \propto N_0 \cdot B^{(\delta+1)/2} \cdot \nu^{-(\delta-1)/2}, \quad (7)$$

where B is the magnetic field strength, ν is the frequency, and δ (with $\alpha = \frac{1-\delta}{2}$) is the slope of the electron energy distribution. For a typical radio spectral index of -1 then $j_R \propto n_{\mathrm{CRe}} \cdot B^2 \cdot \nu^{-1}$ (where n_{CRe} is density of radio-emitting electrons).

The X-ray emissivity, j_X depends on the thermal gas density, n_e^2, and temperature, T_X as

$$j_X \propto n_e^2 \cdot T_X^{1/2}. \quad (8)$$

A linear relation between I_R and I_X implies that the magnetic field and relativistic particles are connected to the thermal electron density as:

$$n_{\mathrm{CRe}} \cdot B^2 \cdot \nu^{-1} \propto n_e^2 \cdot T_X^{1/2}. \quad (9)$$

For example, in the case where the energy density of both radio emitting electrons and magnetic field scale with thermal energy (assuming a quasi-isothermal plasma), the radio emissivity scales with the thermal X-ray emissivity as $j_R/j_X \propto T_X^{1/2}$. Therefore, sublinear slopes suggest that the energy density of radio-emitting electrons and/or that of the magnetic field decline less rapidly than the thermal energy density (e.g., Govoni et al. 2001a). In reacceleration models these trends allow to constrain the way the turbulent energy flux is dampled into relativistic electrons and magnetic fields (Brunetti & Jones 2014). A supperlinear or linear slope is generally expected in the secondary models, depending on the weak and strong magnetic field, as in this case the radio emissivity scales with the thermal X-ray emissivity as $j_R/j_X \propto T_X^{1/2} \cdot B^2/(B^2 + B_{\mathrm{CMB}}^2)$ (e.g., Dolag & Enßlin 2000; Govoni et al. 2001a). The sublinear I_R–I_X scaling in the Abell 2744 halo together with the curved spectra in its subregions, small-scale spectral index fluctuations, steeper spectral indices in the outermost regions, and spectral curvature disfavor secondary models.

Table 6. `Linmix` best fitting parameter of the data for the right panel of Fig. 15 (I_X–α correlation).

	Entire halo	Subcluster 1	Subclusters 2, 3, and 4
$b^{3.0\,\mathrm{GHz}}_{675\,\mathrm{MHz}}$	–	−0.13	0.02
$r_{\mathrm{s},\alpha^{1.5\,\mathrm{GHz}}_{675\,\mathrm{MHz}}}$	0.30 ± 0.08	−0.68 ± 0.08	0.80 ± 0.08
$r_{\mathrm{s},\alpha^{3.0\,\mathrm{GHz}}_{675\,\mathrm{MHz}}}$	0.42 ± 0.14	−0.83 ± 0.08	0.65 ± 0.12

6.2. Spatial correlation between spectral index and X-ray brightness

We study the point-to-point distribution of the halo spectral index with the thermal brightness. To extract the X-ray surface brightness and spectral indices, we again created a grid of cells, see the right panel of Fig. 8. Since the halo is more extended toward lower frequencies, we examine the radio spectral index between $\alpha^{3\,\mathrm{GHz}}_{675\,\mathrm{MHz}}$ and $\alpha^{1.5\,\mathrm{GHz}}_{675\,\mathrm{MHz}}$. The spectral index values are obtained from 15″ resolution radio maps. The regions used for extracting spectral indices between 675 MHz and 3 GHz and the X-ray surface brightness are shown in the right panel of Fig. 6. We considered only regions where the flux density is above 3σ in both the maps, and excluded regions contaminated by discrete point sources.

The resulting α–$I_{\mathrm{X\text{-}ray}}$ distribution for the halo in Abell 2744 is shown in Fig. 15. The halo apparently shows two distinct trends. To check the significance of any correlation, we fit the data assuming a relation of the form:

$$\alpha = a + b \log I_X. \quad (10)$$

The fitting results are given in Table 6 and demonstrate that there is no significant correlation between these two quantities. Given that a positive and negative correlation have been observed for the halo in Abell 2255 (Botteon et al. 2020a) and MACS J0717.5+3745 (Rajpurohit et al. 2020b), respectively, the lack of a significant correlation indicates that this radio halo may be in a different evolutionary state or it may be a multicomponent halo. To check this second possibility, we also fit the data separately. Interestingly, the halo clearly follows two different trends: one section of the halo shows a positive correlation, while the other shows a negative correlation (see Fig. 6). This is the first time that such distinct correlation trends are detected in a